Composites: Part A 184 (2024) 108263

Contents lists available at ScienceDirect

Composites Part A

journal homepage: www.elsevier.com/locate/compositesa

# Assessment of damage sequence in additive manufactured composite laminates under quasi-static out-of-plane loading

A. Fernández *, N. Blanco, D. Trias[1], N. Gascons

*Analysis and Advanced Materials for Structural Design (AMADE), Department of Mechanical Engineering and Industrial Construction, Universitat de Girona, Avda. M. Aurèlia Capmany 61, 17003 Girona, Spain*

ARTICLE INFO

*Keywords:*
Continuous fibre reinforced polymers
3-D printing
Quasi-static indentation
Damage mechanics

ABSTRACT

The understanding of the impact behaviour of additive manufactured continuous fibre reinforced polymers must start from the analysis of the damage mechanisms. In this investigation, the impact damage in a 3D-printed continuous carbon fibre reinforced polymer is studied by means of quasi-static indentation tests. The coupons are manufactured with Fused Filament Fabrication (FFF) using a thermoplastic resin. Three indentation displacement levels were tested, analysing different phases of the impact using X-ray Computed Tomography. The effects of fibre orientation were considered, establishing a comparison between one laminate with conventional orientations (0, 90, ±45) and one with disperse orientations. Results show a progressive damage generation influenced by the inherent defects of the manufacturing process, characterized by delamination growth and stiffness reduction. Fibre and matrix breakage only appear at the final stages when the laminate peak load is reached. The considered dispersed laminate shows less delaminated interfaces compared to the conventional one.

## 1. Introduction

Additive manufacturing (AM) techniques, usually known as 3D printing, are nowadays common in many industrial fields due to their versatility, fast product development, ability to build complex geometries and reduced cost. There is a wide range of available AM technologies in the market, such as Stereolithography (STL), Fused Filament Fabrication (FFF) or Selective Laser Sintering (SLS), among others [1–3]. FFF in particular, which is based on the deposition of thermoplastic filaments layer by layer, is of special interest because of its relative simplicity, versatility and affordability compared to other methods [4]. However, FFF usually induces internal voids at the interfaces between filaments due to lack of compaction and consolidation of the manufactured part after printing, leading to weaker interfacial bonding.

Parts manufactured with FFF usually present low mechanical performance due to the inherent porosity and low mechanical properties of the thermoplastic polymers typically used (i.e., polylactic acid (PLA), acrylonitrile butadiene styrene (ABS), polyamide (PA), etc.). Nevertheless, they can be reinforced to obtain a composite material and reach an acceptable structural performance. In the last decades, some 3D printing technologies have been developed, being able to manufacture parts with polymers reinforced with particles [5], short (chopped) fibres [6,7] or continuous fibres [6,8–10]. The manufacturing of 3D printed continuous fibre reinforced polymers (c-FRP) not only results higher mechanical performance over other reinforcement approaches [11,12], but it also gives flexibility in the fibre orientations. Therefore, it opens the possibility to tailor the 3D printed laminate structure to meet specific design requirements (e.g., in open-hole specimens [13]).

The availability in the market of additive manufacturing c-FRP systems has led to the publication of several studies on the characterization of the mechanical properties of this kind of 3D printed composites. Partially and fully reinforced specimens with continuous carbon and glass fibres manufactured with Markforged® printers [6] have been widely investigated under in-plane tensile tests, analysing the effects of fibre volume fraction and build orientations in the mechanical properties of the printed parts [12,14–19]. In addition to the tensile properties, Justo et al. [14] also determined the compressive strength and stiffness of the Markforged® PA filaments reinforced with glass and carbon fibre. Some studies have also assessed other loading cases such as: bending [17,20,21], interlaminar shear [22,23] or out-of-plane compression [24]. Although clearly improving mechanical performance over unreinforced FFF materials, current 3D printed c-FRP are not yet at the same level as traditionally manufactured pre-pregs. The low fibre volume fraction of the reinforced filaments (around 35% [15,17,25]),

* Corresponding author.
*E-mail address:* alex.fernandez@udg.edu (A. Fernández).
[1] Serra Hunter Fellow.

https://doi.org/10.1016/j.compositesa.2024.108263
Received 1 January 2024; Received in revised form 21 April 2024; Accepted 8 May 2024
Available online 13 May 2024

the inherent presence of voids and lack of interface adhesion result in lower mechanical properties for the additive manufactured specimens. Other studies have analysed the effects on the material microstructure and mechanical performance after post-processing printed parts with hot-press methods [26–30]. The void fraction is considerably reduced when temperature and pressure are applied to the specimens, increasing tensile strength, flexural strength and Mode I interlaminar fracture toughness up 90% in comparison with the non post-processed samples. These findings widen the practical use of additive manufactured composites, as their mechanical performance can be increased with higher fibre volume fraction and reducing void content produced by the manufacturing process. However, these additional steps increase the complexity of the manufacturing process and suppress one of the main points of the 3D printing technology (i.e., the capability to obtain near-neat-shape complex geometric parts without requiring additional molds and post-processing).

Even though some improvement is needed, the promising mechanical performance 3D printed c-FRP and the capacity to build complex geometries without previous molds of FFF technology, have risen interest in its application to the aerospace and automobile industries. However, there is still scarce knowledge about the behaviour of additive manufactured c-FRP under out-of-plane loads and impact events, such as Low-Velocity Impacts (LVI), which are the main compromising events of the components during their service-life. Impact events induce Barely Visible Impact Damage (BVID) in the composite parts (such as delaminations, fibre breakage or matrix cracking), which can lead to a complete structural failure of the affected component or part during its service. The inherent weak interphases between layers of the 3D printed c-FRP and the consequent susceptibility to suffer delaminations have risen the necessity to characterize their interlaminar properties. Recent studies have already assessed the interlaminar fracture toughness of 3D printed c-FRP for Mode I [19,31–37], Mode II [19,31,33,35,36] and Mixed-Mode [33,35].

Furthermore, it is also important to understand the initiation and evolution of the damage mechanisms generated in 3D printed c-FRP during impact events in order to analyse and improve their damage resistance and tolerance. The damage induced during an LVI event can be related to the damage generated in a Quasi-Static Indentation (QSI) test [38], from which we can obtain much more data about the damage sequence. Although some authors have investigated the impact behaviour and resistance of 3D printed c-FRP using either QSI or LVI tests [39–44], they only consider some layers of the printed specimens reinforced with continuous layers. Goh et al. [15] conducted QSI test to quasi-isotropic fully reinforced printed laminate with carbon and glass fibre. They completely perforated 100 × 100 × 1.6 mm specimens with a 13 mm indenter at 1.25 mm/min. However, the samples still were printed with a floor layer of polyamide and the damage mechanisms were not extensively analysed in all the event phases. Caminero et al. [45], on the other hand, used impact Charpy tests to evaluate the impact damage resistance of the 3D printed c-FRP with different reinforcement content. They manufactured multiple specimens reinforced with continuous glass, kevlar and carbon fibres, using two different build orientations, but also leaving polyamide roof and floor layers. The main conclusions from this study stated that impact damage resistance increased as the fibre volume fraction increased, being considerably higher than the usual 3D printed thermoplastics. Even though, the authors also highlighted the need of further investigation on impact performance of additive manufactured composites in order to fully understand their mechanical behaviour.

In view of the scarce investigations available on the literature assessing the impact damage behaviour of 3D printed c-FRP, this current study aims to elucidate how the damage is initiated and propagated in these materials during an impact event. In addition, to the authors knowledge, there are no studies conducted on fully composite 3D printed laminates, and the results obtained so far are always affected by some additional thermoplastic layers, hiding the real performance of the composite material against out-of-plane loads. Taking that into consideration, in this investigation we tested 3D printed continuous carbon fibre reinforced polymers (c-CFRP) laminates under QSI tests at different indentation displacements. Two different layups were assessed to study the effects of fibre orientation and mismatch angle on the impact performance of additive manufactured c-CFRP. No consolidation post-process was considered in this case as the objective is to evaluate the composite laminates manufactured with FFF technology, without avoiding its drawbacks. An extensive analysis of the generated damage at each indentation phase was done with X-ray $\mu$Computed Tomography ($\mu$CT), with the objective to identify the damage mechanisms and damage sequence involved during an impact event in 3D printed composites.

## 2. Materials and methods

In this investigation we used the commercial 3D printer Markforged MarkTwo®, which is able to print continuous fibre reinforced composites. The continuous carbon fibre filament used, c-CFRP, contains a thousand T300 carbon fibres embedded in a thermoplastic matrix (PA) [46]. The most relevant in-plane mechanical properties of the material obtained in previous studies by Iragi et al. [16,31] and Santos et al. [19] are summarized in Table 1. The ply thickness is imposed by the hardware of the printer to 0.125 mm. The specimens were manufactured with a 100% infill of continuous carbon fibre without any PA layers. The base PA layer imposed by the printer was removed before the experimental tests. The printed coupons ready for testing were only composed of 24 c-CFRP layers.

**Table 1**
Most relevant in-plane mechanical properties of the 3D printed c-CFRP ply.

| | |
|---|---|
| Longitudinal elastic modulus, $E_{11}$ | 66 500 MPa [19] |
| Longitudinal tensile strength, $X^t$ | 752 MPa [19] |
| Transversal elastic modulus, $E_{22}$ | 3500 MPa [16] |
| Transversal tensile strength, $Y^t$ | 17.9 MPa [16] |
| Shear modulus, $G_{12}$ | 1910 MPa [16] |
| Shear strength, $S$ | 49 MPa [19] |
| Poisson's ratio, $\nu_{12}$ | 0.39 [19] |

A first batch of specimens was manufactured with a conventional balanced and symmetric quasi-isotropic stacking sequence, i.e. $[45/0/-45/90]_{3s}$. With the aim to check the influence of small mismatch angles between plies in 3D printed c-CFRP and taking the advantage of the manufacturing technique, a second group of coupons was printed considering a dispersed lay-up. We selected a stacking sequence obtained by Sebaey et al. [47] using an ant colony optimization algorithm with the objective to minimize the damaged area: $[10/20/15/10/-80/-85/55/-85/60/-30/-35/-50]_s$. Hereafter, the two different laminate configurations are defined as CON and DISP, respectively. The dimensions of the specimens for the QSI tests were 80 × 80 × 3 mm.

The QSI tests were performed using a 50 kN MTS Insight universal testing machine and an in-house fixture, used in previous works by Wagih et al. [48]. Following the ASTM D6264 standard [49], the indenter was a 12.7 mm diameter hemisphere made of stainless steel and the tests were carried out under displacement control at a loading rate of 0.5 mm/min. The whole experimental setup is illustrated in Fig. 1 with the indenter, the specimen location and the fixture. The specimen was placed centred between the two rectangular adapters with a 50 mm diameter hole. The adapters along with the specimen were centred and clamped between the fixture plates (upper and lower plate in Fig. 1) to prevent separation of the edges from the base while loading. Then the whole assembly was mounted and fixed on the testing machine assuring that the indentation load was applied on the centre of the specimen.

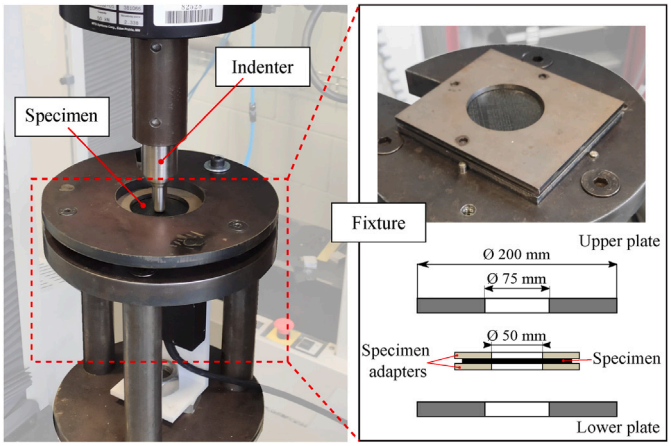


**Fig. 1.** Experimental QSI setup.

The test campaign was conducted in two principal phases. Initially, a QSI test was performed until complete perforation for each laminate in order to detect the different damage stages. Then, based on each laminate response, 3 different displacement levels were defined. The considered displacements were $d = 0.9$, 2.4 and 3.5 mm for laminate CON and $d = 0.7$, 1.5 and 3 mm for laminate DISP (Fig. 3). One specimen per displacement level was used for each stacking sequence.

Additionally, the analytical calculation of the delamination threshold load was also performed to compare with the experimental results. The expression that gives the required load to generate a delamination in the laminate is [50]:

$$F_{dn} = \pi \sqrt{\frac{32 D^* G_{IIc}}{n+2}} \tag{1}$$

where $D^*$ is the effective bending stiffness, $G_{IIc}$ the fracture toughness in mode II loading and $n$ the number of evenly distributed delaminations. For generating the first delamination, $n = 1$.

For the inspection after the QSI tests, it is worth mentioning that C-Scan turned out to be unsuccessful because of the inherent porosity in the material [28]. Therefore, each coupon was inspected using the X-ray $\mu$CT technique, which allowed to capture the different failure mechanisms and damage extension and through-the-thickness location. The inspection equipment used were an X-ray source with 20 W of power and 5 µm focal spot, and a detector of 2400 × 2400 pixel (Fig. 2).

First, the whole area of the tested specimens was inspected to capture the total extent of the delaminations. The coupons were stacked together in triplets, analysing them in a single operation with the following inspection parameters: 55 kV voltage, 155 µA intensity, 84 mm field of view (FOV) and 37.5 µm voxel size. Afterwards, in order to reduce the width to thickness ratio of the panels during the X-ray inspection and improve image resolution (i.e. reducing voxel size), the specimens were cut to 15 × 80 mm keeping the indentation point centred. These inspections were made stacking the coupons by pairs with the next parameters: 40 kV voltage, 110 µA intensity, 20.75 mm FOV and 9.3 µm voxel size. In all cases, 1800 projections were acquired (with 3 integrations per projection) while rotating the samples 360°. In addition, raw specimens (with no indentation applied) were also inspected to analyse the initial microstructure of the laminates before any damage is generated.

## 3. Results and discussion

### 3.1. Damage sequence

The load–displacement curves from the complete QSI test until perforation for CON and DISP laminates are shown in Fig. 3. In general terms, the response of each load–displacement curve is characterized by an initial elastic increase of the load followed by a smooth stiffness loss. After this first slope change, the load keeps increasing monotonically until a sudden load drop is recorded. Finally, after the first drop, the load presents a plateau-shaped development until the laminates are completely perforated.

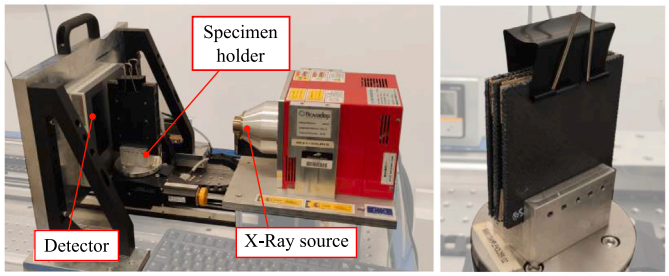


**Fig. 2.** General view of the X-ray $\mu$CT setup, left, and detail of a triplet stacking of QSI specimens ready for inspection, right.

From the laminates load–displacement curves of the full QSI tests and following a similar procedure as Wagih et al. [51], the indentation process can be divided into five stages, from I to V. As previously mentioned, three different indentation displacements were selected in function of the defined stages to carry out partial QSI tests for each type of laminate. The results of the load–displacement curves of the partial QSI batches for CON and DISP laminates with their corresponding stages are shown in Fig. 4. At a glance, all the curves show a similar general tendency. However, some dispersion can be noticed, as each curve does not exactly overlap the one with lower indentation displacement.

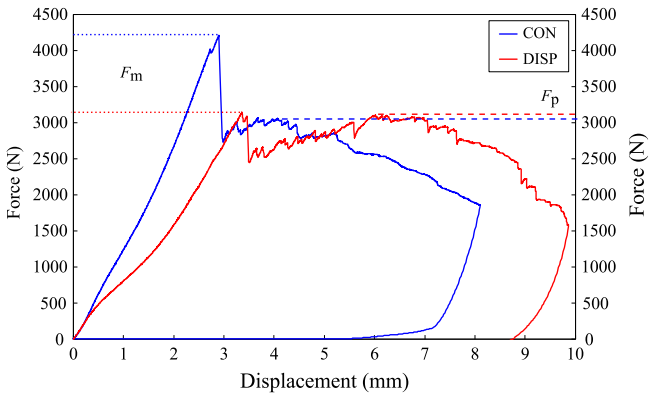


**Fig. 3.** QSI load–displacement curves until complete perforation of the laminates, for each stacking sequence. The horizontal dotted lines indicate the maximum peak load ($F_m$) and the dashed lines the perforation load ($F_p$).

For every QSI test with its corresponding indentation displacement $d$, the experimental values of the maximum load ($F_m$) and the perforation load ($F_p$) are presented in Tables 2 and 3 for the CON and DISP laminates, respectively. Values of total ($E_T$), absorbed ($E_D$) and elastic ($E_E$) energies along with the projected damaged area ($A$) are also listed in the same tables. The total energy has been calculated by integrating the whole area below the load–displacement curve, while the elastic energy has been computed integrating only the unloading curve. The absorbed energy is then obtained subtracting the elastic energy from the total energy. The analytic $F_{d1}$ results obtained using Eq. (1) for each laminate are compared in Table 4 with the mean value of the experimental peak load.

Results of the non-destructive inspection with $\mu$CT technique of the raw specimens and after each level of indentation show the damage generated inside the laminates (Figs. 5 to 7). From these tomographies,

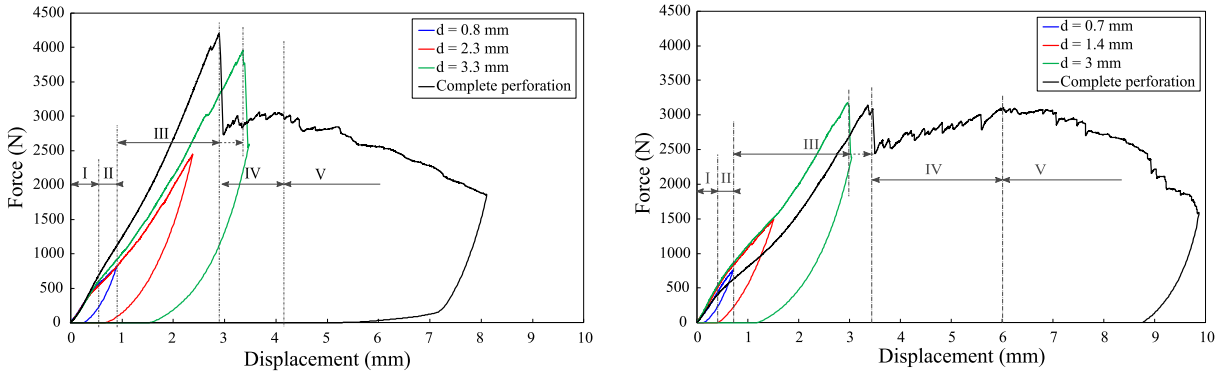


**(a)** Conventional (CON) laminate **(b)** Dispersed (DISP) laminate

**Fig. 4.** Load–displacement curves from the QSI tests for CON and DISP laminates, at different indentation levels. The established damage stages are depicted for each stacking sequence.

**Table 2**
QSI test results for CON laminate.

| $d$ (mm) | Stage | $F_m$ (N) | $F_p$ (N) | $E_T$ (J) | $E_D$ (J) | $E_E$ (J) | $A$ (mm$^2$) |
|---|---|---|---|---|---|---|---|
| 0.9 | II | 820.5 | – | 0.41 | 0.21 | 0.20 | – |
| 2.4 | III | 2453.7 | – | 2.73 | 1.33 | 1.40 | 237.2 |
| 3.5 | IV | 3953.0 | – | 6.18 | 4.99 | 2.19 | 684.7 |
| 8.1 | V | 4204.7 | 3065.9 | 19.14 | 18.32 | 0.83 | – |

**Table 3**
QSI test results for DISP laminate.

| $d$ (mm) | Stage | $F_m$ (N) | $F_p$ (N) | $E_T$ (J) | $E_D$ (J) | $E_E$ (J) | $A$ (mm$^2$) |
|---|---|---|---|---|---|---|---|
| 0.7 | II | 759.7 | – | 0.27 | 0.10 | 0.17 | – |
| 1.5 | III | 1500.1 | – | 1.24 | 0.60 | 0.64 | 159.9 |
| 3.0 | IV | 3179.8 | – | 4.64 | 3.41 | 1.23 | 605.6 |
| 9.9 | V | 3139.1 | 3104.6 | 22.29 | 21.76 | 0.53 | – |

**Table 4**
Comparison of experimental peak load results and analytical delamination threshold load using Eq. (1) of CON and DISP laminates.

| Lay-up | Exp. peak load (N) | $F_{d1}$ (N) |
|---|---|---|
| CON | 4078.9 (±125.9) | 3412.2 |
| DISP | 3159.5 (±20.4) | 3040.4 |

the damage sequence can be summarized in the following steps. In the undamaged specimens, we can already observe voids generated between filaments (Fig. 5). These voids grow and merge, creating first micro-delaminations at $d$ = 0.8 and 0.7 mm for CON and DISP laminates, respectively. Then, delaminations propagate and spread until $d$ = 3.3 and 3 mm in CON and DISP, respectively. Noticeable fibre breakage and matrix cracking appear at these levels of indentation, matching with the first load drop of the load–displacement curves. Beyond this point, all the damage mechanisms have occurred and the damage in the laminates is already extensive and catastrophic. Therefore, no more $\mu$CT were taken at further displacement levels because it would not add any valuable information.

### 3.2. Stage I. Elastic regime

The first stage of the load–displacement curves corresponds to an elastic response until a change in the slope is detected, indicating a stiffness loss in the laminate. This behaviour lasts until 0.5 mm and 0.3 mm in CON and DISP laminates, respectively. Fig. 3 shows that the curves of the two laminates overlap during this first stage, which proves that both lay-ups have practically equal bending stiffness and in-plane properties.

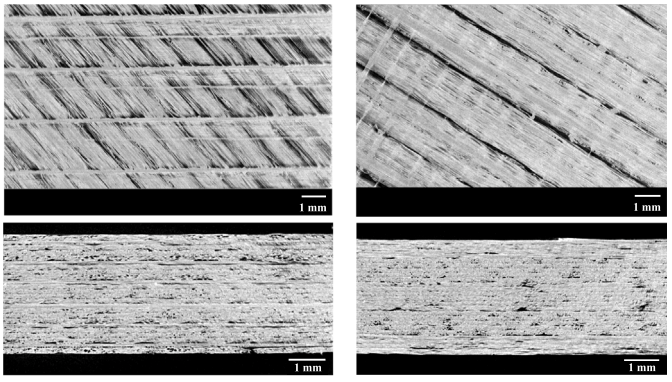


**(a)** Conventional (CON) laminate **(b)** Dispersed (DISP) laminate

**Fig. 5.** In-plane (top) and cross-section (bottom) $\mu$CT images obtained from manufactured panels before testing (no indentation applied).

There is no evidence of damage generation during this elastic stage, which is mainly dominated by the increase of indentation load following the Hertzian contact mechanics theory. Therefore, this stage can also be represented by the $\mu$CT of the raw specimens (Fig. 5). However, the micro-structure of both 3D printed laminates already presents voids before applying any load. These defects are inherent of the manufacturing process, generated between the filaments deposited by the printer nozzle. The void content was measured in 1700 cross-sections from the raw $\mu$CT scans of each laminate, obtaining a mean value of 8.7% (±2.11) and 11.2% (±0.46), for CON and DISP laminate, respectively. These results are in the same range of values previously reported in other studies [14,25,29,52]. In the CON laminate cross-section shown in Fig. 5(a), the measured void content is 11.7%, pointing out the higher variability of the porosity throughout the cross-sections. Moreover, in CON laminate, voids are smaller and evenly distributed in the cross-section, as the mismatch angle between layers is 45° in all the interphases. In contrast, the DISP laminate has smaller mismatch angles, generating zones with concentrated and larger voids while other zones are richer in material as it can be seen in the cross-section of Fig. 5(b), with a porosity of 11.1%. Focusing on the interphase between layers shown in the in-plane views of Fig. 5, continuous periodic lines with no material (darker zones) can be observed between the filaments (lighter zones).

### 3.3. Stage II. Stiffness loss

After the first elastic stage, a smooth decrease in the slope is present in both tested laminates, which indicates a stiffness loss. This second

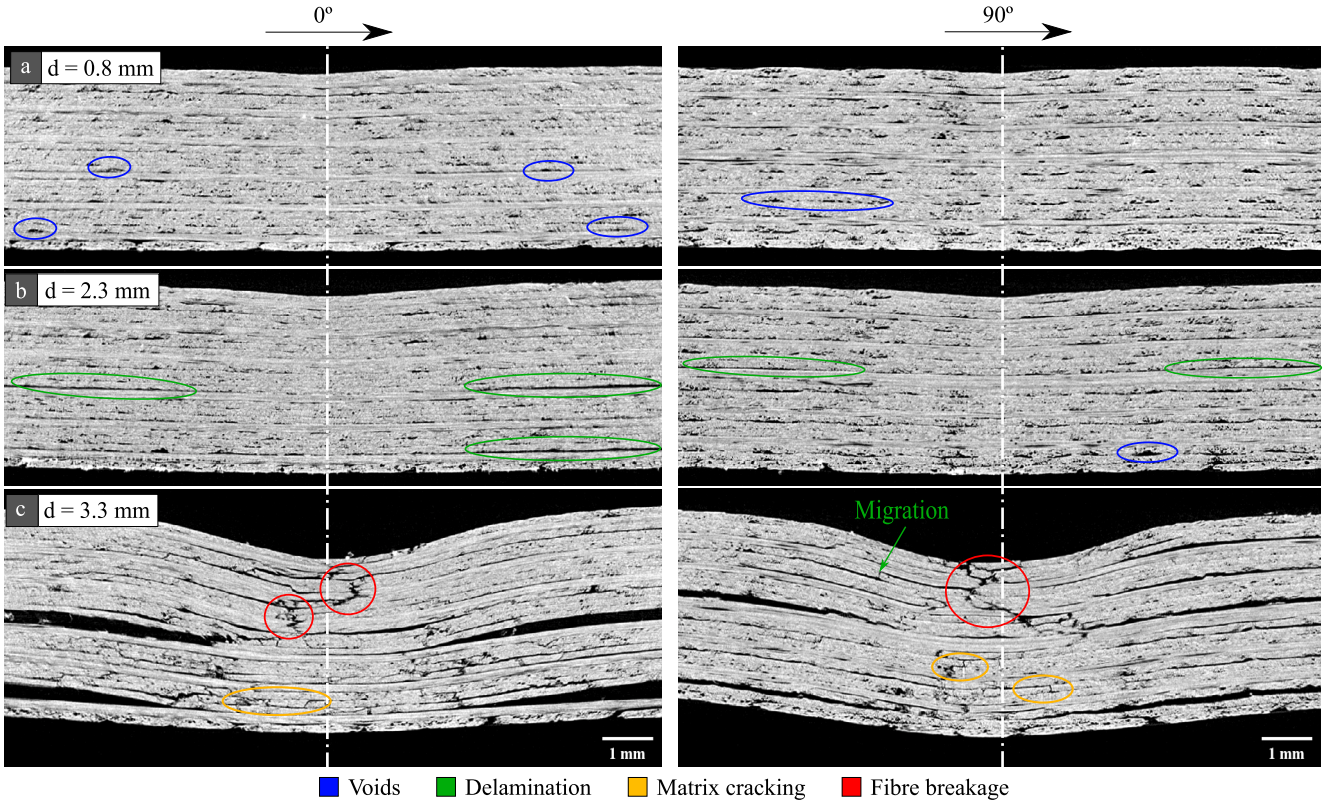


**Fig. 6.** $\mu$CT images of the cross-sections of 3 different specimens of type CON at different displacement levels.

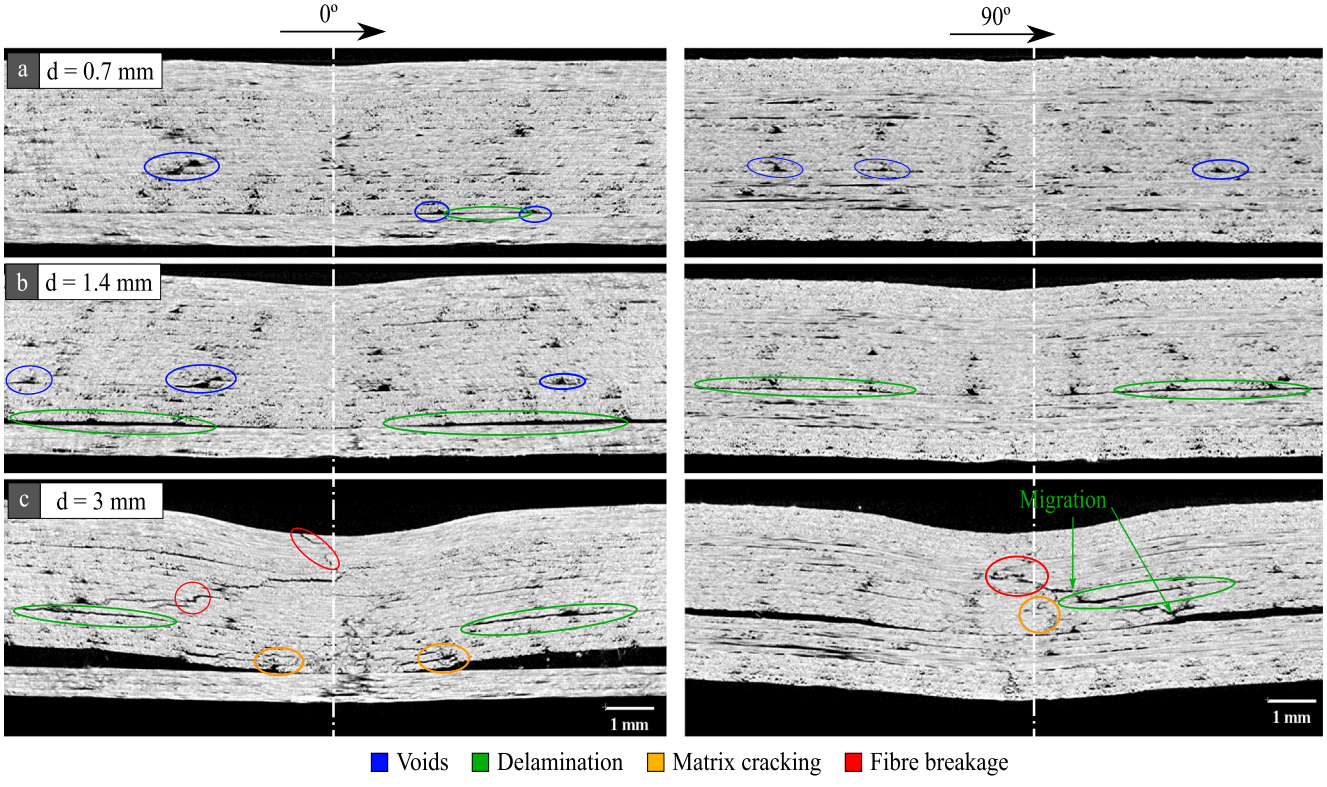


**Fig. 7.** $\mu$CT images of the cross-sections of 3 different specimens of type DISP at different displacement levels.

stage begins with the slope change at 0.5 mm and 0.3 mm, and ends at 0.9 mm and 0.7 mm in CON and DISP laminates, respectively. The damage of this stage is mainly dominated by the voids already present before indentation inside both laminates, as shown in Figs. 6(a) and 7(a). Moreover, at this level of displacements, the voids show a subtle tendency to grow and merge. The merging of the neighbouring voids as the load increases leads to the creation of micro-delaminations in the bottom half of the laminates (Figs. 6(a) and 7(a)), which cause the characteristic stiffness reduction of this stage. The apparition of delaminations in rich void zones of the interfaces is an evidence that these imperfections are acting as delamination onsets.

### 3.4. Stage III. Propagation

The third stage occurs between 0.9 mm to 3.3 mm, and from 0.7 mm to 3.4 mm, for CON and DISP laminates, respectively. It initiates after the first decrease in the slope of the load–displacement curves. The end of this stage is defined at the peak force value, just before the first load drop occurs. During this period, the response of the laminates is also linear but with slope, or stiffness, higher than that of Stage II. Nevertheless, the stiffness in this stage is lower than for Stage I due to the damage already generated inside the laminate. At the end of the stage, a stiffness growth can also be observed due to geometric non-linearities (membrane effect), caused by the deformation already produced to the specimens during the indentation. Although the peak load takes place at different displacement values for each specimen due to stiffness dispersion during Stage II, their values are in the same order of magnitude with a mean of 4078.9 (±125.9) N and 3159.5 (±20.4) N for CON and DISP laminates, respectively.

This stage is mainly driven by the propagation of already created delaminations and generation of new ones, as it is shown in Figs. 6(b) and 7(b). It can be seen that for CON laminate, larger delaminations are generated at −45/0 interfaces in the bottom half of the laminate, while smaller ones start to appear at −45/90 interphases in the top half. In the DISP laminate, however, only two delaminations are visible in the bottom half of the laminate, where the mismatch angle between layers is greater (i.e. 90°). For both laminates, most of the delaminations appear at interphases where voids already started to grow and merge in previous indentation displacements. No matrix cracking or fibre breakage is observed up to this level of indentation, also revealed by the smooth response of the load–displacement curve, without any load drop characteristic of these kind of damage mechanisms.

Taking into account these results, it can be concluded that the progressive stiffness loss observed in the tests is related to the progressive opening and joining of the inter-filament voids, caused by the shear stresses due to contact and bending. At the same time, delaminations are mainly onset by these voids, propagating the damage mostly along the central laminate interfaces where the shear due to bending is higher.

### 3.5. Stage IV. Extensive damage generation

Stage IV is represented by a large sudden load drop in the load–displacement curves. The ranges of displacement of this stage are 3 mm to 4.1 mm and 3 mm to 6 mm for CON and DISP laminates, respectively. At the beginning of this stage a large load drop is observed, which is related to multiple fibre breakage and matrix cracking as it can be seen in the $\mu$CT images at d = 3.3 mm (Fig. 6(c)) and d = 3 mm (Fig. 7(c)) for CON and DISP laminates, respectively. Even though this load drop takes place at a different displacement level for each tested coupon due to dispersion, the peak force causing the drop remains in the same order of magnitude, as has been stated in Section 3.4. After the first and more pronounced drop, the load follows a plateau-shaped response with a saw-tooth pattern (small load drops), until it reaches the perforation load value ($F_p$). For the DISP laminate this stage is considerably larger, with a wider range of displacement to reach $F_p$.

In the $\mu$CT inspections of the CON laminate just after the first load drop (Fig. 6(c)), extensive damage is already observable. Many fibre breakage is present on the top-half of the laminate. Smaller delaminations also appear in the same zone, migrating between interfaces. On the other hand, matrix cracking appears at the bottom-half layers, where the tensile stresses are higher due to bending. The damage that started to generate in Stage III at the top-half of the CON laminate evolved to three delaminations, equally spaced and located between the −45/90 layers. The main and larger delaminations in the CON laminate, already present in the previous stage, are found at interface 14 and 22, between −45/0 layers.

In the case of the DISP laminate (Fig. 7(c)), the damage mechanisms found are similar to those found in the CON laminate. However, the crack density and the number of delaminated interfaces are larger in the CON laminate. In the upper part of the DISP laminate, we can observe small fibre breakage, which is mainly generated due to compressive stresses. In the mid-part some fibre breakage is also present as well as small delaminations, which are connected through the thickness (migration between interfaces). Delaminations observed at Stage III in the lower part at 15 and 20 interphases have grown, becoming the main delaminated interphases of the DISP laminate. Moreover, matrix cracking is also observable in 18th and 19th layers.

### 3.6. Stage V. Perforation

Stage V goes from 4.1 mm and 6 mm until the end of the test, for CON and DISP laminates, respectively. This stage begins when the local maximum load, termed as perforation load ($F_p$), is reached. From this point, the load continuously decreases as the displacement keeps advancing until the laminate is completely perforated. Inspections with X-ray $\mu$CT were not made for this stage because extensive and critical damage was already observed in the previous stage for both laminates.

### 3.7. Damage summary

A general overview of the sequence of damage events with their corresponding load–displacement curves is summarized in Fig. 8, for both 3D printed laminates. Each stage of the curve is represented with a different colour, also used to represent the corresponding damage mechanisms in the schematic drawing below. From the test results, X-ray $\mu$CT observations and the analysis carried out in the previous sections, we can establish a general sequence of events as: (i) inherent defects and voids in the material act as delamination onsets, starting micro-delaminations; (ii) micro-delaminations merge and grow forming larger delaminations, while new ones are also generated; (iii) fibre breakage and matrix cracking are generated in the laminate; (iv) complete failure and perforation of the laminate. This damage sequence illustrates the expected behaviour of the CON and DISP 3D printed laminates under low-velocity events [53–55].

### 3.8. Laminate layup comparison

Despite CON and DISP laminates show a similar behaviour and damage sequence under QSI tests, subtle differences in the results have been noticed and pointed out in Sections 3.2 to 3.5.

The damage onset and development is mainly governed by the voids present in the material. As previously mentioned, each layup has different distribution and dimensions of voids (Fig. 5). The CON laminate presents an even distribution with smaller voids along the cross-section, which leads to the creation of damaged interfaces also evenly distributed along the thickness (Fig. 6). On the other hand, we observe larger and localized voids in the DISP laminate. In this case, the damage interfaces are concentrated in some of the interfaces rather than being distributed (Fig. 7). Looking at the indentation displacements in Figs. 6(b) and Fig. 7(b), we observe that in the DISP laminate we find larger delaminations at a lower displacement than

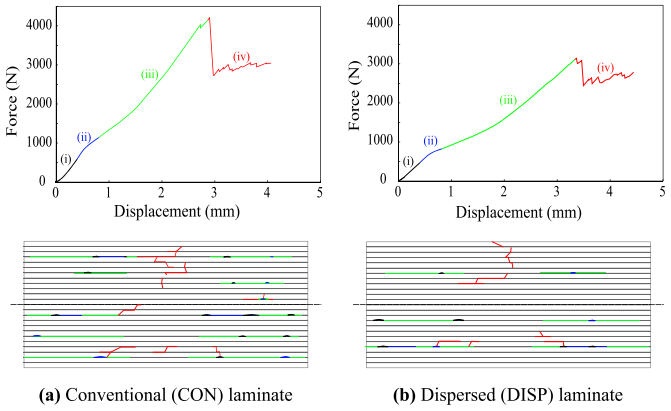


**(a)** Conventional (CON) laminate **(b)** Dispersed (DISP) laminate

**Fig. 8.** Schema of the sequence of the damage mechanisms generated in the laminates during the QSI tests and their corresponding location in the load–displacement curves: (i) inherent defects and voids; (ii) onset of micro-delaminations; (iii) merge and growth of delaminations; (iv) fibre breakage and matrix cracking.

**Table 5**
Comparison of experimental and analytical stiffness of CON and DISP laminates.

| Lay-up | Exp. stiffness (N/mm) | Analytical stiffness (N/mm) |
|---|---|---|
| CON | 1065.2 (±20.9) | 1223.6 |
| DISP | 1203.3 (±91.6) | 1296.6 |

in the CON laminate. In comparison, the CON layup developed more damaged interfaces even though they are of a smaller size.

In this case, we do not observe the characteristic initial load drop when the damage onset occurs [48,56], which can be related to the delamination threshold load $F_{d1}$. Instead, the response observed in this study is a smooth stiffness reduction due to the apparition of micro-delaminations from voids and there is no initial load drop to compare with the analytical $F_{d1}$. Even though, it can be noticed that the stiffness reduction takes place at considerably lower values of the indentation load than the calculated values of $F_{d1}$. Therefore, it can be said that the high void content reduces the load at which the damage onset appears.

Furthermore, the theoretical effective stiffness due to bending and shear $K_{bs} = (K_b K_s)/(K_b + K_s)$ gives the linear relationship between load and indentation displacement. The constants $K_b$ and $K_s$ are the bending and shear stiffnesses, respectively, and are given by Shivakumar et al. [57]. The analytical stiffness values of each laminate are compared with the experimental stiffness of the elastic regime (stage I) in Table 5. The predicted values of the stiffness overestimate the experimental results, also indicating a knockdown effect of the porosity in the stiffness of the laminates.

Fig. 9 shows the variation of the total energy and the elastic and dissipated energy contribution at different displacement levels. Total energy is represented as the sum of the two energy components. In Stage II (d = 0.9 mm and d = 0.7 mm for CON and DISP laminates, respectively) the amount of energy is evenly shared between dissipated energy and elastic energy, which means that some damage is already generated despite being a mainly elastic behaviour. This correlates with the change in the slope in the load–displacement curves, probably caused by the delamination onsets in the voids. For larger displacements (Stage III), when the total amount of energy is higher, the contribution of both energy components is still evenly split. This is explained by the damage development throughout this stage (contributing to energy dissipation) while the load–displacement trend remains mostly linear, which keeps contributing to the elastic energy component. After the first load drop, there is a large increase of the dissipated energy, driven by the fibre breakage and cracks observed in Figs. 6(c) and 7(c). The elastic component, instead, shows a more subtle growth. The magnitude of energy involved in the system is larger for the CON laminate in all terms. This is because laminate with conventional orientations shows higher maximum load capacity than the DISP laminate, storing more energy. Furthermore, the load drop of the CON laminate is nearly the double of that of the DISP laminate, which is directly related to a higher level of energy dissipation.

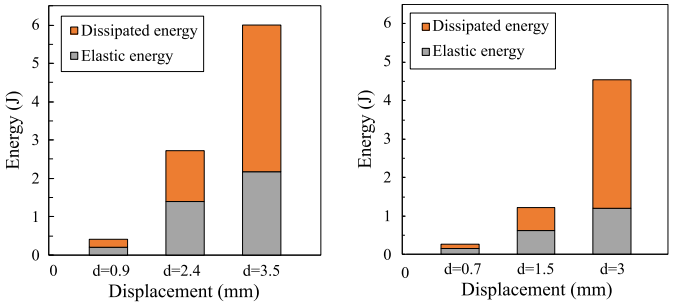


**(a)** CON laminate **(b)** DISP laminate

**Fig. 9.** Contribution of the elastic and dissipated energies at each displacement level. Sum of elastic and dissipated energies represents the total energy.

The damage extension evolution for both laminates is represented in Fig. 10 as the projected delaminated areas at two different characteristic events of the load–displacement curve: before the stiffness recovery during Stage III (Fig. 10(a, b)) and just after the first load drop at the beginning of Stage IV (Fig. 10(c, d)). These projections clarify and confirm the growth of the delaminations during Stage III as previously stated in Section 3.4. The total damaged area just after fibre breakage is larger for CON laminate (10.7% of the total area of the specimen) in comparison with the damaged area in DISP laminate at the same damage event (9.46%).

A tridimensional view of the delaminated interfaces after the first load drop is represented in Fig. 11, where the extent and orientation of each damaged interface is shown. It can be observed that CON laminate presents a larger number of delaminated interphases through all the thickness, while DISP laminate only show delaminations at the bottom part. In both cases, delaminations are oriented following the same orientation as the lower layer of the interface. In the of the DISP laminates it can be seen that damage is prone to happen where the mismatch angle between layers is larger. This could explain the fewer number of delaminations in DISP laminate, which are concentrated only on the interphases with larger mismatch angle [47,56,58].

## 4. Conclusions

An experimental campaign of quasi-static indentation tests has been carried out on Markforged® 3D printed continuous carbon/polyamide laminates to identify the sequence of the damage mechanisms during out-of-plane loading. Specimens with 100% of layers reinforced with c-CFRP were considered. A conventional balanced and symmetric quasi-isotropic (CON) laminate has been compared with laminate with dispersed orientations (DISP): $[10/20/15/10/-80/-85/55/-85/60/-30/-35/-50]_s$. This comparison allowed to assess the influence of the layup orientation in the impact response of this type of material. X-ray computed tomography inspections before applying indentation determined the presence of voids in the material, inherent to the manufacturing process. The results obtained with the non-destructive inspections after indentation combined with the load–displacement curves from the tests allowed to define a damage sequence summarized in five main stages. Stage I corresponds to the initial elastic behaviour of the laminates with no evidence of generated damage. The damage onset occurs during Stage II, along with stiffness loss. The already present voids grow and merge, acting as delamination onsets. Stage III is characterized by damage propagation with delaminations growing and spreading until fibre breakage develops, leading to a drastic drop

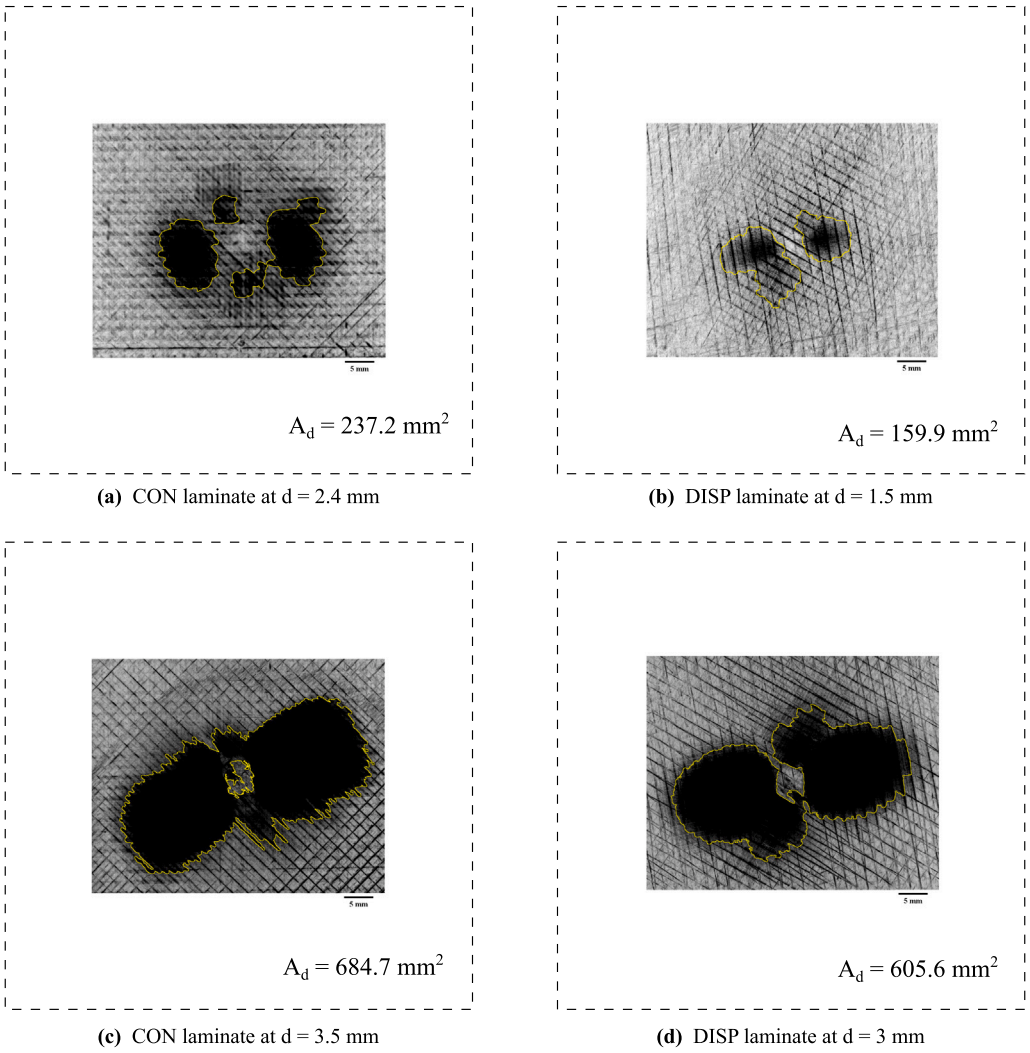


**(a)** CON laminate at d = 2.4 mm **(b)** DISP laminate at d = 1.5 mm

**(c)** CON laminate at d = 3.5 mm **(d)** DISP laminate at d = 3 mm

**Fig. 10.** Projected delaminated area (delimited in yellow) for CON and DISP laminates during Stage III (a, b) and just after fibre breakage(c, d). The perimeter of the specimens is represented with a dashed-square for reference.

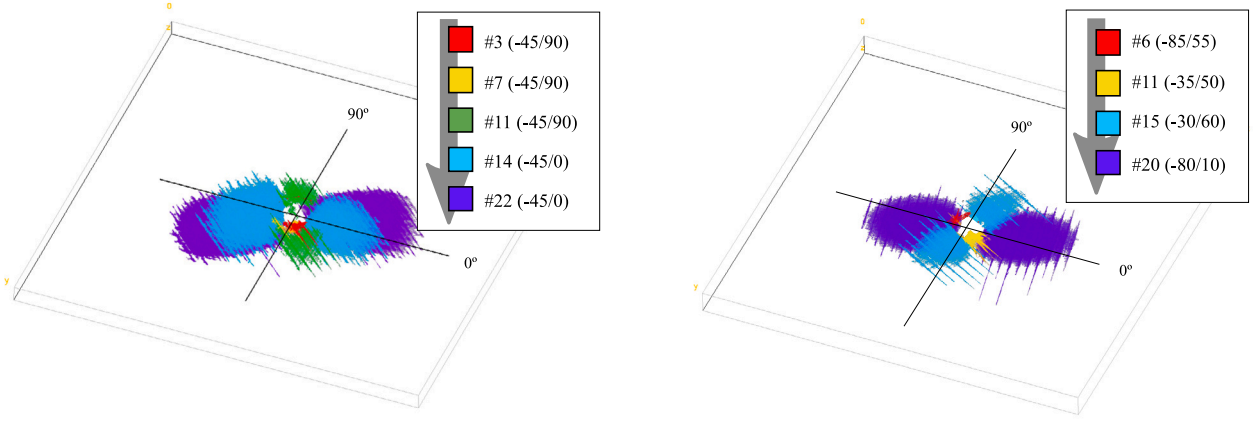


**(a)** CON laminate damaged interfaces **(b)** DISP laminate damaged interfaces

**Fig. 11.** 3D representation of the main damaged interfaces after the first load drop detected in the load–displacement curves. The volumes containing the damage represent the laminate dimensions of 80 × 80 mm.

load in the experimental curves. From this point extensive damage and matrix and fibre breakage happen during Stage IV until perforation load is reached, Stage V.

From the comparison between the two type of laminates, we can say that there is an effect of the stacking sequence on the quasi-static indentation response of this type of materials. The delaminations grow earlier in the DISP layup, but the CON laminate ends having a larger number of damaged interfaces, leading to a larger damaged area. In addition, CON laminate shows a 29.1% higher peak load.

Results of this work point out the influence of the internal defects generated by the additive manufacturing process. The voids between the printed filaments are acting as delamination onsets, becoming a key factor on the impact performance of the laminates. A reduction of the void volume fraction might help to delay the delamination onset and improve the impact performance of these type of additive manufactured composite laminates.

## CRediT authorship contribution statement

**A. Fernández:** Writing – original draft, Validation, Methodology, Investigation, Formal analysis, Data curation, Conceptualization. **N. Blanco:** Writing – review & editing, Validation, Supervision, Resources, Project administration, Methodology, Funding acquisition, Conceptualization. **D. Trias:** Writing – review & editing, Validation, Supervision, Resources, Project administration, Methodology, Funding acquisition, Conceptualization. **N. Gascons:** Writing – review & editing, Validation, Supervision.

## Declaration of competing interest

The authors declare that they have no known competing financial interests or personal relationships that could have appeared to influence the work reported in this paper.

## Data availability

The raw/processed data required to reproduce these findings can be obtained from the corresponding author upon request.

## Acknowledgements

This research was funded by the Spanish Ministry of Science, Innovation and Universities (MCIU), the Spanish Research Agency (AEI) and the European Regional Development Fund (FEDER, UE) (grant no. RTI2018-094435-B-C32 and PID2022-140343NB-I00). The first author also acknowledges the support from the Catalan Government through contract no. FI2021-B-00939.Open Access funding provided thanks to the CRUE-CSIC agreement with Elsevier.

## References

[1] Conner BP, Manogharan GP, Martof AN, Rodomsky LM, Rodomsky CM, Jordan DC, Limperos JW. Making sense of 3-D printing: Creating a map of additive manufacturing products and services. Addit Manuf 2014;1–4:64–76. http://dx.doi.org/10.1016/j.addma.2014.08.005.

[2] Guo N, Leu MC. Additive manufacturing: technology, applications and research needs. Front Mech Eng 2013;8(3):215–43. http://dx.doi.org/10.1007/s11465-013-0248-8.

[3] Ngo TD, Kashani A, Imbalzano G, Nguyen KTQ, Hui D. Additive manufacturing (3D printing): A review of materials, methods, applications and challenges. Composites B 2018;143:172–96. http://dx.doi.org/10.1016/j.compositesb.2018.02.012.

[4] Penumakala PK, Santo J, Thomas A. A critical review on the fused deposition modeling of thermoplastic polymer composites. Composites B 2020;201:108336. http://dx.doi.org/10.1016/j.compositesb.2020.108336.

[5] Griffini G, Invernizzi M, Levi M, Natale G, Postiglione G, Turri S. 3D-printable CFR polymer composites with dual-cure sequential IPNs. Polymer 2016;91:174–9. http://dx.doi.org/10.1016/j.polymer.2016.03.048.

[6] Markforged, Inc.. 2023, URL: https://markforged.com/es/materials/continuous-fibers/continuous-carbon-fiber, [Accessed 12 December 2023].

[7] Christian P, Jones IA, Rudd CD, Campbell RI, Corden TJ. Monomer transfer moulding and rapid prototyping methods for fibre reinforced thermoplastics for medical applications. 2001, p. 969–76, 32.

[8] Anisoprint, SARL. 2023, URL: https://anisoprint.com/, [Accessed 12 December 2023].

[9] 9TLabs, AG. 2023, URL: https://www.9tlabs.com/, [Accessed 12 December 2023].

[10] Desktop Metal., Inc.. 2023, URL: https://www.desktopmetal.com/, [Accessed 12 December 2023].

[11] Wang X, Jiang M, Zhou Z, Gou J, Hui D. 3D printing of polymer matrix composites: A review and prospective. Composites B 2017;110:442–58. http://dx.doi.org/10.1016/j.compositesb.2016.11.034.

[12] Blok LG, Longana ML, Yu H, Woods BKS. An investigation into 3D printing of fibre reinforced thermoplastic composites. Addit Manuf 2018;22:176–86. http://dx.doi.org/10.1016/j.addma.2018.04.039.

[13] Zappino E, Filippi M, Pagani A, Petiti M, Carrera E. Experimental and numerical analysis of 3D printed open-hole plates reinforced with carbon fibers. Composites C 2020;2:100007. http://dx.doi.org/10.1016/j.jcomc.2020.100007.

[14] Justo J, Távara L, García-Guzmán L, París F. Characterization of 3D printed long fibre reinforced composites. Compos Struct 2018;185:537–48. http://dx.doi.org/10.1016/J.COMPSTRUCT.2017.11.052, Publisher: Elsevier.

[15] Goh GD, Dikshit V, Nagalingam AP, Goh GL, Agarwala S, Sing SL, Wei J, Yeong WY. Characterization of mechanical properties and fracture mode of additively manufactured carbon fiber and glass fiber reinforced thermoplastics. Mater Des 2018;137:79–89. http://dx.doi.org/10.1016/j.matdes.2017.10.021.

[16] Iragi M, Pascual-González C, Esnaola A, Lopes CS, Aretxabaleta L. Ply and interlaminar behaviours of 3D printed continuous carbon fibre-reinforced thermoplastic laminates; effects of processing conditions and microstructure. Addit Manuf 2019;30:100884. http://dx.doi.org/10.1016/J.ADDMA.2019.100884, Publisher: Elsevier.

[17] Chacón JM, Caminero MA, Núñez PJ, García-Plaza E, García-Moreno I, Reverte JM. Additive manufacturing of continuous fibre reinforced thermoplastic composites using fused deposition modelling: Effect of process parameters on mechanical properties. Compos Sci Technol 2019;181:107688. http://dx.doi.org/10.1016/j.compscitech.2019.107688.

[18] Todoroki A, Oasada T, Mizutani Y, Suzuki Y, Ueda M, Matsuzaki R, Hirano Y. Tensile property evaluations of 3D printed continuous carbon fiber reinforced thermoplastic composites. Adv Compos Mater 2020;29(2):147–62. http://dx.doi.org/10.1080/09243046.2019.1650323.

[19] Santos JD, Fernández A, Ripoll L, Blanco N. Experimental characterization and analysis of the in-plane elastic properties and interlaminar fracture toughness of a 3D-printed continuous carbon fiber-reinforced composite. Polymers 2022;14(3):506. http://dx.doi.org/10.3390/POLYM14030506, Publisher: Multidisciplinary Digital Publishing Institute.

[20] Swart R, Korkees F, Dorrington P, Thurman J. Evaluation of the impact performance and energy absorption capabilities of 3D printed composites. Rapid Prototyp J 2022;28(9):1636–54. http://dx.doi.org/10.1108/RPJ-10-2021-0287, Publisher: Emerald Publishing Limited.

[21] Chen J, Ghimire S. 3D printing continuous fibre reinforced and biomimicked layered composites with enhanced damage resilience. Compos Struct 2022;296:115854. http://dx.doi.org/10.1016/j.compstruct.2022.115854.

[22] Caminero MA, Chacón JM, García-Moreno I, Reverte JM. Interlaminar bonding performance of 3D printed continuous fibre reinforced thermoplastic composites using fused deposition modelling. Polym Test 2018;68:415–23. http://dx.doi.org/10.1016/j.polymertesting.2018.04.038.

[23] Yavas D, Zhang Z, Liu Q, Wu D. Interlaminar shear behavior of continuous and short carbon fiber reinforced polymer composites fabricated by additive manufacturing. Composites B 2021;204:108460. http://dx.doi.org/10.1016/j.compositesb.2020.108460.

[24] Yogeshvaran RN, Liu BG, Farukh F, Kandan K. Out-of-plane compressive response of additively manufactured cross-ply composites. J Mech 2020;36(2):197–211. http://dx.doi.org/10.1017/jmech.2019.59.

[25] Chabaud G, Castro M, Denoual C, Le Duigou A. Hygromechanical properties of 3D printed continuous carbon and glass fibre reinforced polyamide composite for outdoor structural applications. Addit Manuf 2019;26:94–105. http://dx.doi.org/10.1016/j.addma.2019.01.005.

[26] Saeed K, McIlhagger A, Harkin-Jones E, McGarrigle C, Dixon D, Ali Shar M, McMillan A, Archer E. Characterization of continuous carbon fiber reinforced 3D printed polymer composites with varying fibre volume fractions. Compos Struct 2022;282:115033. http://dx.doi.org/10.1016/j.compstruct.2021.115033.

[27] Pascual-González C, San Martín P, Lizarralde I, Fernández A, León A, Lopes CS, Fernández-Blázquez JP. Post-processing effects on microstructure, interlaminar and thermal properties of 3D printed continuous carbon fibre composites. Composites B 2021;210:108652. http://dx.doi.org/10.1016/j.compositesb.2021.108652.

[28] Garoz Gómez D, Pascual-González C, García-Moreno Caraballo J, Fernández-Blázquez JP. Methodology to design and optimise dispersed continuous carbon fibre composites parts by fused filament fabrication. Composites A 2023;165:107315. http://dx.doi.org/10.1016/j.compositesa.2022.107315.

[29] He Q, Wang H, Fu K, Ye L. 3D printed continuous CF/PA6 composites: Effect of microscopic voids on mechanical performance. Compos Sci Technol 2020;191:108077. http://dx.doi.org/10.1016/j.compscitech.2020.108077.
[30] Hetrick DR, Sanei SHR, Ashour O. Void content reduction in 3D printed glass fiber-reinforced polymer composites through temperature and pressure consolidation. J Compos Sci 2022;6(5):128. http://dx.doi.org/10.3390/jcs6050128, Number: 5 Publisher: Multidisciplinary Digital Publishing Institute.
[31] Iragi M, Pascual-Gonzalez C, Esnaola A, Aurrekoetxea J, Lopes C, Aretxabaleta L. Characterization of elastic and resistance behaviours of 3D printed continuous carbon fibre reinforced thermoplastics. 2020, p. 8.
[32] Touchard F, Chocinski-Arnault L, Fournier T, Magro C, Lafitte A, Caradec A. Interfacial adhesion quality in 3D printed continuous CF/PA6 composites at filament/matrix and interlaminar scales. Composites B 2021;218:108891. http://dx.doi.org/10.1016/j.compositesb.2021.108891.
[33] Kong X, Luo J, Luo Q, Li Q, Sun G. Experimental study on interface failure behavior of 3D printed continuous fiber reinforced composites. Addit Manuf 2022;59:103077. http://dx.doi.org/10.1016/j.addma.2022.103077.
[34] Dang Z, Cao J, Pagani A, Zhang C. Fracture toughness determination and mechanism for mode-I interlaminar failure of 3D-printed carbon-Kevlar composites. Compos Commun 2023;39:101532. http://dx.doi.org/10.1016/j.coco.2023.101532.
[35] Katalagarianakis A, Polyzos E, Van Hemelrijck D, Pyl L. Mode I, mode II and mixed mode I-II delamination of carbon fibre-reinforced polyamide composites 3D-printed by material extrusion. Composites A 2023;173:107655. http://dx.doi.org/10.1016/j.compositesa.2023.107655.
[36] Polyzos E, Katalagarianakis A, Van Hemelrijck D, Pyl L. Delamination analysis of 3D-printed nylon reinforced with continuous carbon fibers. Addit Manuf 2021;46:102144. http://dx.doi.org/10.1016/j.addma.2021.102144.
[37] Santos JD, Guerrero JM, Blanco N, Fajardo JI, Paltán CA. Numerical and experimental analysis of the mode I interlaminar fracture toughness in multidirectional 3D-printed thermoplastic composites reinforced with continuous carbon fiber. Polymers 2023;15(10):2403. http://dx.doi.org/10.3390/polym15102403, Number: 10 Publisher: Multidisciplinary Digital Publishing Institute.
[38] Nettles A, Douglas M. A comparison of quasi-static indentation testing to low velocity impact testing. In: Zureick A, Nettles A, editors. Composite materials: testing, design, and acceptance criteria. 100 Barr Harbor Drive, PO Box C700, West Conshohocken, PA 19428-2959: ASTM International; 2002, p. 116–116–15. http://dx.doi.org/10.1520/STP10634S.
[39] Dikshit V, Nagalingam A, Goh G, Agarwala S, Yeong W, Wei J. Quasi-static indentation analysis on three-dimensional printed continuous-fiber sandwich composites. J Sandw Struct Mater 2021;23(2):385–404. http://dx.doi.org/10.1177/1099636219836058.
[40] Wang K, Li S, Wu Y, Rao Y, Peng Y. Simultaneous reinforcement of both rigidity and energy absorption of polyamide-based composites with hybrid continuous fibers by 3D printing. Compos Struct 2021;267:113854. http://dx.doi.org/10.1016/j.compstruct.2021.113854.
[41] Wang K, Zhu W, Li S, Peng Y, Ahzi S. Investigations of quasi-static indentation properties of 3D printed polyamide/continuous Kevlar/continuous carbon fiber composites. J Appl Polym Sci 2022;139(32):e52758. http://dx.doi.org/10.1002/app.52758, _eprint: https://onlinelibrary.wiley.com/doi/pdf/10.1002/app.52758.
[42] Zhu W, Li S, Peng Y, Wang K, Ahzi S. Effect of continuous fiber orientations on quasi-static indentation properties in 3D printed hybrid continuous carbon/Kevlar fiber reinforced composites. Polym Adv Technol 2023;34(5):1565–74. http://dx.doi.org/10.1002/pat.5991, _eprint: https://onlinelibrary.wiley.com/doi/pdf/10.1002/pat.5991.
[43] Papa I, Manco E, Epasto G, Lopresto V, Squillace A. Impact behaviour and non destructive evaluation of 3D printed reinforced composites. Compos Struct 2022;281:115112. http://dx.doi.org/10.1016/j.compstruct.2021.115112.
[44] Kabir SM, Mathur K, Seyam AFM. Impact resistance and failure mechanism of 3D printed continuous fiber-reinforced cellular composites. J Text Inst 2021;112(5):752–66. http://dx.doi.org/10.1080/00405000.2020.1778223, Publisher: Taylor & Francis.
[45] Caminero MA, Chacón JM, García-Moreno I, Rodríguez GP. Impact damage resistance of 3D printed continuous fibre reinforced thermoplastic composites using fused deposition modelling. Composites B 2018;148:93–103. http://dx.doi.org/10.1016/J.COMPOSITESB.2018.04.054, Publisher: Elsevier.
[46] TORAYCA Carbon Fiber, Toray Composite Materials America. 2022, URL: https://www.toraycma.com/products/carbon-fiber/, [Accessed 03 May 2022].
[47] Sebaey TA, González EV, Lopes CS, Blanco N, Costa J. Damage resistance and damage tolerance of dispersed CFRP laminates: Design and optimization. Compos Struct 2013;95:569–76. http://dx.doi.org/10.1016/j.compstruct.2012.07.005.
[48] Wagih A, Maimí P, Blanco N, Costa J. A quasi-static indentation test to elucidate the sequence of damage events in low velocity impacts on composite laminates. Composites A 2016;82:180–9. http://dx.doi.org/10.1016/j.compositesa.2015.11.041, Publisher: Elsevier Ltd.
[49] ASTM D 6264 – 98 (reapproved 2004). Standard test method for measuring damage resistance of fiber-reinforced polymer-matrix composite to concentrated quasi-static indentation. 2004.
[50] Olsson R. Analytical prediction of damage due to large mass impact on thin ply composites. Composites A 2015;72:184–91. http://dx.doi.org/10.1016/j.compositesa.2015.02.005.
[51] Wagih A, Maimí P, González EV, Blanco N, De Aja JR, De La Escalera FM, Olsson R, Alvarez E. Damage sequence in thin-ply composite laminates under out-of-plane loading. Composites A 2016;87:66–77. http://dx.doi.org/10.1016/J.COMPOSITESA.2016.04.010, Publisher: Elsevier.
[52] Lupone F, Padovano E, Venezia C, Badini C. Experimental characterization and modeling of 3D printed continuous carbon fibers composites with different fiber orientation produced by FFF process. Polymers 2022;14(3):426. http://dx.doi.org/10.3390/polym14030426, Number: 3 Publisher: Multidisciplinary Digital Publishing Institute.
[53] Abisset E, Daghia F, Sun XC, Wisnom MR, Hallett SR. Interaction of inter- and intralaminar damage in scaled quasi-static indentation tests: Part 1 – Experiments. Compos Struct 2016;136:712–26. http://dx.doi.org/10.1016/j.compstruct.2015.09.061.
[54] Olsson R. Mass criterion for wave controlled impact response of composite plates. Composites A 2000;31(8):879–87. http://dx.doi.org/10.1016/S1359-835X(00)00020-8.
[55] Bull DJ, Spearing SM, Sinclair I. Investigation of the response to low velocity impact and quasi-static indentation loading of particle-toughened carbon-fibre composite materials. Composites A 2015;74:38–46. http://dx.doi.org/10.1016/j.compositesa.2015.03.016.
[56] Wagih A, Maimí P, Blanco N, García-Rodríguez SM, Guillamet G, Issac RP, Turon A, Costa J. Improving damage resistance and load capacity of thin-ply laminates using ply clustering and small mismatch angles. Composites A 2019;117(April 2018):76–91. http://dx.doi.org/10.1016/j.compositesa.2018.11.008, Publisher: Elsevier.
[57] Shivakumar KN, Elber W, Illg W. Prediction of impact force and duration due to low-velocity impact on circular composite laminates. J Appl Mech 1985;52(3):674–80. http://dx.doi.org/10.1115/1.3169120.
[58] Lopes CS, Seresta O, Coquet Y, Gürdal Z, Camanho PP, Thuis B. Low-velocity impact damage on dispersed stacking sequence laminates. Part I: Experiments. Compos Sci Technol 2009;69(7):926–36. http://dx.doi.org/10.1016/j.compscitech.2009.02.009.